OCEANOGRAPHY

Winter in the coastal ocean: Seasonal freezing causes seafloor expansion and contraction

Alexandre Normandeau[1]*, Barret L. Kurylyk[2], Emma J. Harrison[3], Haley D. Geizer[3], Genevieve Philibert[1], Robert Way[4], Christopher L. Algar[3], Zachary MacMillan-Kenny[5], Jennifer L. Eamer[1,6], Nicolas Van Nieuwenhove[6], Jordan B. R. Eamer[1], Liz Pijogge[7], Frédéric Cyr[5], Ian Church[8], Eric Oliver[3], Michelle Saunders[7], Audrey Limoges[6]

Seafloor mapping in polar regions has led to the recognition of landforms associated with subsea permafrost. Despite recent studies indicating rapid subsea permafrost degradation, information on seasonal seafloor changes remains limited. Here, we use time-lapse multibeam bathymetry (2021–2024) and bottom-water temperature data to reveal seasonal formation and degradation of small frost blisters (5 meters wide and 20 to 50 centimeters high) as ice forms within surficial sediments. These frost blisters were degraded in October 2021 at depths of ≤25 meters but were widespread in July 2023. They thawed between July and November 2023, reformed over the following winter, and were present again in August 2024. Data from moored bottom-water sensors and sediment cores indicate that the formation and degradation of frost blisters are driven by seasonal temperature changes at depth and influenced by freshened porewater in surficial sediments. This study documents previously unrecognized seasonal expansion and contraction of the seafloor driven by freeze-thaw cycles of freshened porewater.

INTRODUCTION

Permafrost is a large component of the Arctic's cryosphere (*1*) and is critical for global carbon dynamics (*2*), terrestrial hydrology including groundwater-surface water interactions (*3*), ground mechanics and associated terrestrial and marine infrastructure design (*4*), and the functioning of marine ecosystems (*5*). Subsea permafrost has received considerably less attention than its terrestrial counterpart, in part due to the challenges of mapping and directly monitoring it. Defined by perennially frozen sediments beneath the seabed, subsea permafrost is often a remnant of past glaciations when continental shelves were exposed to the atmosphere but have since become submerged due to postglacial sea level rise (*6*). Ice-bonded subsea permafrost is preserved because of bottom water temperatures below the freezing point of freshened porewater (*7*–*9*) and likely exists along many Arctic and subarctic coastlines (Fig. 1A) (*8*). Therefore, the preservation of subsea permafrost is facilitated where cold bottom waters exist and either (i) where a sea-level lowstand allowed permafrost to form on continental shelves and be preserved during the postglacial transgression (*6*) or (ii) where submarine groundwater flows toward the seabed in the coastal ocean, flushes out the salt, and freezes at ambient temperatures close to 0°C (*8*).

Unlike terrestrial permafrost, the thermal regime of subsea permafrost is influenced by the overlying seawater, which introduces unique thermal dynamics due to the attenuated seasonal amplitude of bottom seawater temperature variations compared to land surface temperatures and due to salt intrusion into surficial sediments (*10*). Salt diffusion and brine flows can overcome the freshening influence of groundwater discharge, depressing the freezing point and leading to thawing of surficial permafrost without changes in the bottom water thermal regime (*10*). Subsea permafrost has been studied using geophysical and hydroacoustic techniques (*11*–*13*), and recent work in the Canadian Beaufort Sea has shown that subsea permafrost thaw can create craters up to 28 m deep in less than a decade, in part due to saltwater intrusion (*13*). This pronounced seabed change poses a major geohazard for offshore infrastructure, such as subsea telecommunication cables, subsea pipelines, and offshore renewable energy infrastructure (*13*).

A unique aspect of terrestrial permafrost is the seasonal freezing and thawing of the active layer due to surface energy exchanges (*14*). Active layer dynamics can be associated with important geohazards in terrestrial environments (*15*, *16*). The active layer, defined as the uppermost section of ground that undergoes seasonal freeze-thaw above permafrost (*15*), also serves as the primary zone for subsurface hydrologic routing of water in the summer (*17*). In nonpermafrost regions, seasonal ground freezing is also well-documented (*18*) and also leads to ground heaving and instabilities. Although seasonal ground freezing and active layer processes have been extensively studied in terrestrial environments, the dynamics of seasonal freeze-thaw cycles and its influence in subsea geomorphology remain largely unexplored (*19*, *20*). Subsea active layer dynamics are likely critical for seafloor stability in these environments and for mediating summertime sediment porewater exchanges that are known to affect biogeochemical processes and benthic ecosystems at lower latitudes (*21*). In marine environments, active layer processes and seasonal freezing remain poorly understood because of the absence of fine-scale geomorphological mapping, insufficient in situ monitoring of subsea sediment thermal regimes, and the scarcity of repeated seafloor mapping of subsea permafrost processes (*13*).

This study provides evidence for seasonal freeze-thaw cycles in surficial sediments of subsea thermokarst environments. Through a

[1]Geological Survey of Canada (Atlantic), Bedford Institute of Oceanography, Dartmouth, Nova Scotia , Canada. [2]Department of Civil and Resource Engineering and Centre for Water Resources Studies, Dalhousie University, Halifax, Nova Scotia , Canada. [3]Department of Oceanography, Dalhousie University, Halifax, Nova Scotia, Canada. [4]Northern Environmental Geoscience Laboratory, Department of Geography and Planning, Kingston, Ontario, Canada. [5]Centre for Fisheries and Ecosystem Research, Fisheries and Marine Institute of Memorial University, St. John's, Newfoundland and Labrador, Canada. [6]Department of Earth Sciences, University of New Brunswick, Fredericton, New Brunswick, Canada. [7]Lands and Natural Resources, Nunatsiavut Government, Nain, Newfoundland and Labrador, Canada. [8]Department of Geomatics and Geodesy Engineering, University of New Brunswick, Fredericton, New Brunswick, Canada.
*Corresponding author. Email: alexandre.normandeau@nrcan-rncan.gc.ca

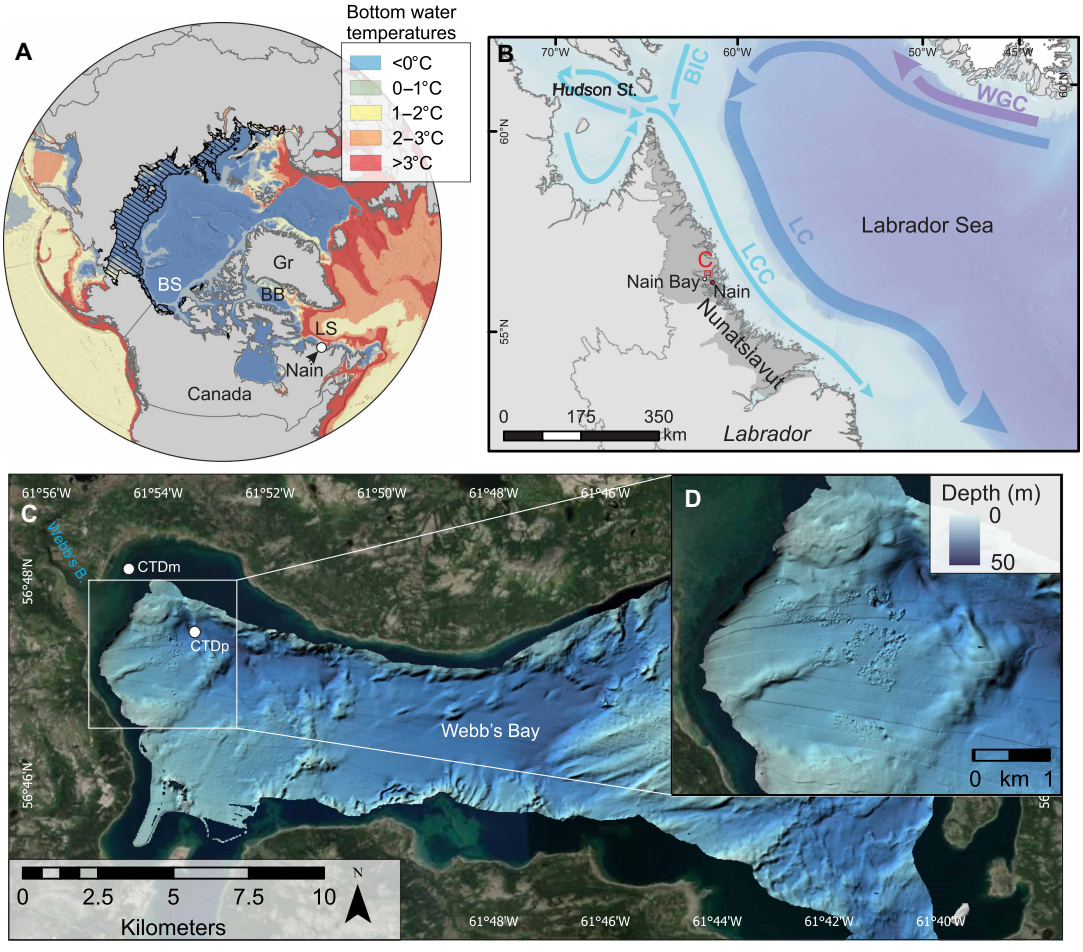

Fig. 1. Location of Webb's Bay, Nunatsiavut. (**A**) Average annual bottom water temperature distribution in the northern hemisphere [modified from (*8*)]. BS, Beaufort Sea; Gr, Greenland; BB, Baffin Bay; LS, Labrador Sea. Hashed polygons represent the modeled distribution of subsea permafrost from (*49*). (**B**) Main surface ocean currents along Nunatsiavut, Labrador, including the West Greenland Current (WGC), Baffin Island Current (BIC), Labrador Current (LC), and Labrador coastal current (LCC). (**C**) Webb's Bay bathymetry with inset (**D**) illustrating the subsea thermokarst landforms. Ship-based conductivity-temperature-depth profiles (CTDp) are shown in Fig. 9B. A moored CTD (CTDm) over an annual cycle at 18-m depth is shown in Fig. 9A.

combination of hydroacoustic surveys, sediment core analyses, and in situ bottom water temperature measurements, we identified distinct seasonal patterns associated with freeze-thaw cycles. Our findings indicate that seasonal ground freezing in the coastal ocean exhibits dynamic thermal behavior akin to terrestrial environments, albeit influenced by marine conditions and submarine groundwater discharge (SGD). We examine the mechanisms driving active layer dynamics and seasonal ground freezing and discuss the broader implications for the stability of subsea environments.

Regional setting

The coastline of Labrador mostly consists of igneous and metamorphic bedrock. The bedrock is overlain by extensive blankets of till that were deposited under the Laurentide Ice Sheet during its retreat during the late Pleistocene or early Holocene (*22*). Layers of medium- to fine-grained marine and glaciomarine sediments were also deposited below the late Pleistocene marine limit, which attained 40 to 100 m along the Labrador Coast (*22*, *23*).

Webb's Bay is located near the community of Nain, Nunatsiavut, in northern Labrador, Canada (Fig. 1). Webb's Bay is in the Nain coast ecodistrict in the coastal barrens ecozone and is characterized by a series of west-to-east fjords and sheltered bays, with dozens of small islands. The rugged topography creates a dissected coastline with many "narrows," confined channels through which strong tidal currents flow. The strong tidal currents in those narrows allow the movement of water from the Labrador Shelf to the coastal environment of Nain. Cold waters in the region form during winter due to energy loss to the atmosphere. This layer remains below the seasonally warmed surface waters after the onset of spring, forming the cold intermediate layer (CIL). The CIL on the Labrador Shelf lies between 25 and 200 m deep and generally remains below 0°C for most of the year (*24*). In addition to being formed locally during the winter, it is continuously combined with Arctic-origin waters carried southward by the Labrador coastal current (LCC), so that the coldest temperatures in the core of the CIL are often found in July or August. The LCC is a branch of the Labrador Current system and is formed by a mixture of the Baffin Island Current and outflow from the Hudson Strait (*25*). Between the end of the summer and the beginning of the winter, the CIL is gradually eroded and mixed with the warmer surface layer by the strong winds generally

prevailing in the fall. The consequence of this mixing is a gradual increase in temperature at the depth range generally occupied by the CIL.

High-resolution multibeam bathymetry and subbottom profiles collected in Webb's Bay revealed the presence of a subsea thermokarst environment (Fig. 1) (*8*). Collapsed mounds with 1- to 2-m-high rims and chaotic seabed expression of mounds and depression with 2 m of seabed relief were mapped in 2021. These thermokarst landforms are in 20- to 40-m water depth and are associated with SGD and cold bottom waters.

RESULTS

Seafloor landforms

Seafloor landforms of Webb's Bay were identified through a combination of high-resolution (30-cm horizontal resolution) multibeam bathymetry imagery and seafloor photographs. The landforms are described in Fig. 2 and below, and their distribution is illustrated in Fig. 3.

Pockmarks

Three different sizes of circular seafloor depressions (pockmarks) were identified from multibeam bathymetry and seafloor photos (Fig. 2). The smallest pockmarks, identified as micropockmarks on seafloor imagery, are about 10 cm wide and 1 to 2 cm deep (Fig. 4A). They are observed in seafloor imagery by their darker color compared to the surrounding sediment. The brown coloration of the depressions can be attributed to microalgal growth. Microalgal growth could be present because of the influx of nutrients from the seepage at each depression. Alternatively, these depressions could be due to bioturbation. These pockmarks are assumed to be present in all water depths of Webb's Bay.

The intermediate size pockmarks, referred to as small pockmarks in Fig. 4B, are 1 to 2 m wide and 5 to 10 cm deep. These pockmarks are widespread in water depths of 0 to 20 m (Fig. 3A). The larger-sized pockmarks, which are referred to as regular "pockmarks" in Fig. 4C, are 5 to 10 m wide and 20 to 30 cm deep. These pockmarks are observed overprinting the small ones. In backscatter, they are characterized by higher intensities (Fig. 4D), reflecting coarser sediment at the seabed. Seafloor imagery shows that higher intensity is characterized by cobbles at the seafloor, surrounded by mud. These pockmarks are located where the subbottom stratigraphy shows a thinning of Holocene sediment and where underlying glacial material nearly outcrops near the surface (Fig. 4E).

	Feature type	Geomorphology	Water depth	Size (*D* by *H*)	Origin
SGD	Micropockmarks		0–30 m	*D* = 10 cm *H* = 1–2 cm	Freshwater seepage
SGD	Small pockmarks		0–20 m	*D* = 1–2 m *H* = 5–10 cm	Freshwater seepage
SGD	Pockmarks	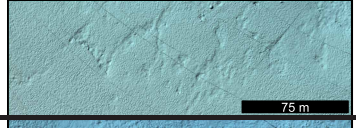	0–20 m	*D* = 5–10 m *H* = 20–30 cm	Enhanced freshwater seepage
Seasonal freezing	Frost blisters	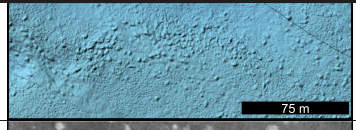	15–30 m	*D* = 5 m *H* = 30–50 cm	Seasonal ice formation
Seasonal freezing	Sorted polygons?		15–30 m	*D* = 2–7 m *H* = 0 cm	Seasonal differential frost heave
Seasonal freezing	Frost heave terrain	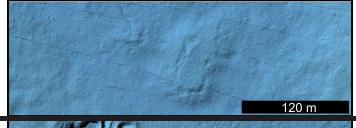	15–30 m	*D* = NA *H* = <1 m	Seasonal heaving
Permafrost	Frost mound	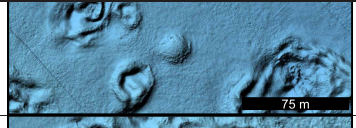	20–30 m	*D* = 20 m *H* = 1–3 m	Permafrost mounds
Permafrost	Thermokarst	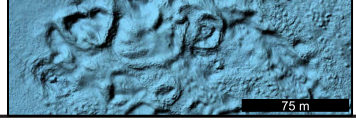	20–30 m	*D* = > 20 m *H* = 3–5 m	Degraded permafrost

Fig. 2. Summary of SGD to permafrost landforms observed in Webb's Bay [diameter (*D*) and height (*H*)] and their interpreted origin. NA, not applicable.

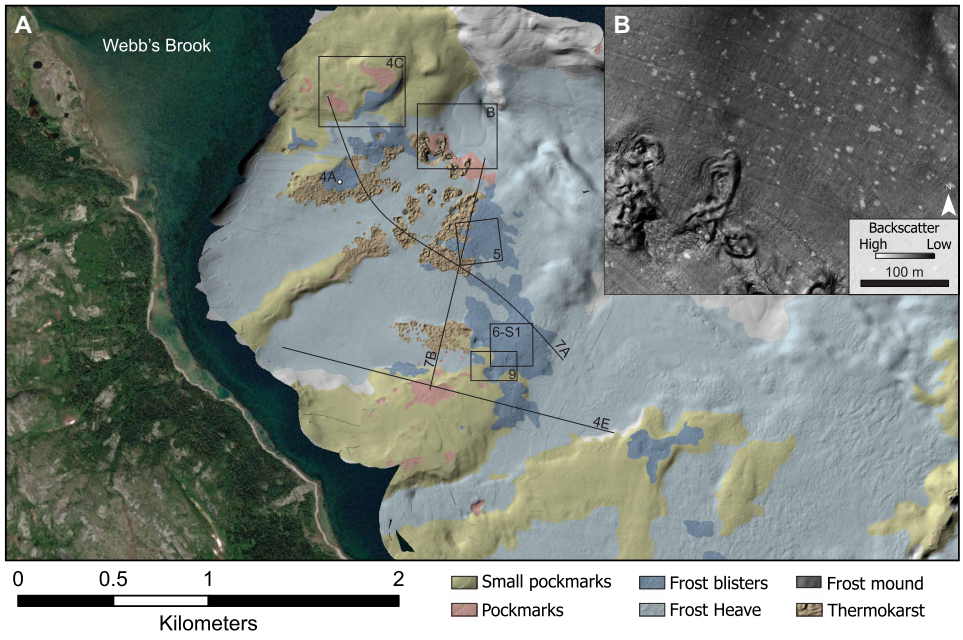

Fig. 3. Surficial geology of Webb's Bay. Surficial geomorphology interpretation of the head of Webb's Bay illustrating the variety of seeping and cryospheric structures on the seabed. Light gray is normal background seafloor without evidence of seepage or cryospheric landforms. Box and transect numbers refer to the figures further in the manuscript. (**B**) Backscatter imagery of a deeper area of Webb's Bay [inset in (**A**)], illustrating higher reflectivity polygons on the seafloor.

Mounds and heaved terrain

The July 2023 bathymetric survey revealed the widespread presence of hundreds of small mounds (termed blisters, ~5 m wide by 20 to 50 cm high) on the seafloor of Webb's Bay (Figs. 2, 3A, 5, and 6). The average volume of individual blisters is ~1 m^3. They were present at depths ranging from 15 to 30 m in areas of pockmarks and within and near the thermokarst area. Blisters exhibit a lower backscatter intensity compared to the surrounding sediment (fig. S1), which is interpreted as consisting of higher mud and/or water content in the surficial sediment.

Between 15- and 40-m water depth, 2- to 7-m wide high-reflectivity backscatter polygons are observed (Figs. 2, 3B, and 4D). These polygons do not correspond to any morphological changes in the 30-cm bathymetry grid (Fig. 4, C and D). While less densely distributed than the blisters, these polygons are dispersed throughout the area. Their higher backscatter intensity suggests that they consist of gravel and cobble in a predominantly muddy environment. The seafloor surrounding the blisters is slightly chaotic, with elongated mounds and linear depressions (Figs. 2 and 5C). These features have less than 1-m relief and can be found in water depths of 15 to 30 m (frost heave in Fig. 3A). These features have no clear backscatter response.

Seasonal seafloor changes

Repeat bathymetric surveys (2021–2024) of Webb's Bay reveal that the first-order landforms, i.e., the larger ones (Fig. 2) described as subsea thermokarst (*8*), remained stable between 2021 and 2024 (Fig. 5). In contrast, smaller features such as blisters (5 m wide and 20 to 50 cm high) and heaving landforms exhibited seasonal variability.

The November 2021 survey showed fewer blisters compared to the next July 2023 survey. Blisters were absent in areas shallower than 25 m in 2021, whereas they are abundant in July 2023 (Figs. 5 and 6). In the 25- to 30-m-depth range, blisters are present in November 2021, although they appear attenuated compared to July 2023 (Fig. 5, A and B). By July 2023, blisters are abundant throughout the head of Webb's Bay, occurring in waters as shallow as 15 m (Fig. 3A and 6B). By November 2023, blisters were greatly diminished (Figs. 5C and 6C). Instead, the seafloor was cratered with small depressions, elongated cracks, and heaved terrain (Figs. 5C and 6C). Ten months later, in August 2024, blisters reappeared across all depth ranges (Figs. 5D and 6D). Although some new blisters were created, most emerged at locations nearby and at previous occurrences, as evidenced by the backscatter data (fig. S1). The backscatter data also show that, despite the seasonal appearance and disappearance of blisters, their low-intensity signature persisted throughout all seasons (fig. S1).

Frozen sediment in the subsurface

In July 2023, sediment cores were collected over the area of these small blisters. Some cores contained ice lenses, some of which were clear of sediment (Fig. 7, C and D) (*8*). A piston core collected from the thermokarst area (Core 97PC, 130.5 cm long; Fig. 7, B to D) penetrated one of these lenses, and holes were drilled in the core upon recovery to assess the presence of ice. The upper section (45.5 cm long), believed to contain ice, was kept frozen, while the lower section (85 cm long) was kept at 4°C. Potential ice layers in the lower section may have thawed during storage at 4°C. Nevertheless, the core shows that the upper ice lens contains irregular reticulate cryostructures, resembling those described in (*8*) from a core collected in 2022. The lenticular cryostructures observed at the top and bottom of the upper core section are attributed to freezing during storage, whereas reticulate cryostructures represent undisturbed subseafloor conditions. The core shows that ice lenses are present

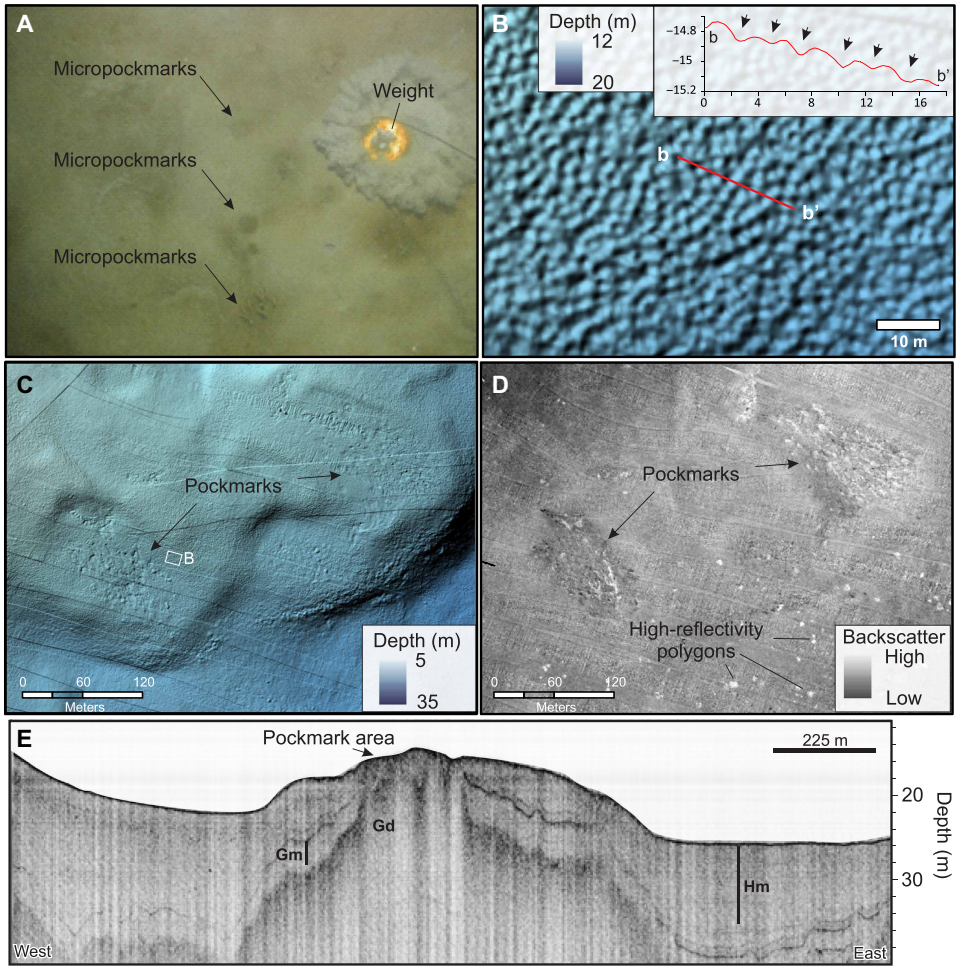

Fig. 4. Pockmark observed in Webb's Bay. (**A**) Micropockmarks identified in seafloor imagery. Orange weight in imagery is 10 cm across and its impact on the seabed produced the sediment cloud. Location in Fig. 3A. (**B**) Small pockmarks distributed throughout Webb's Bay (see Fig. 3A for distribution). (**C**) Pockmarks on Webb's Brook delta. Location in Fig. 3A. (**D**) Backscatter imagery of the same pockmarks as in (C) illustrating the higher intensity of the center of the pockmarks presumably reflecting coarser sediment at the seabed. (**E**) Subbottom profile illustrating the near outcropping of glacial diamict (Gd) where the pockmarks form. Gm, glaciomarine mud; Hm, Holocene mud. Location of profile in Fig. 3A.

within the first 50 cm of the subseafloor. However, high-amplitude reflections in subbottom profiles suggest that the permafrost table in Webb's Bay may occur deeper, at 1 to 2 m below the surface (Fig. 7, A and B). Therefore, the cored ice lenses are unlikely to represent permafrost conditions associated with the high reflectivity in the subseabed (*8*). Instead, these ice lenses are more likely associated with seasonal dynamics and the formation of the small blisters described above.

Porewater of sediment cores

Porewater analyses were completed on thirteen sediment cores from Webb's Bay (Fig. 8). The cores were retrieved from various seafloor conditions, including thermokarst landforms, pockmarks, and undisturbed areas. Despite the diverse sampling locations, porewater salinity trends, estimated from the chloride content, were similar across cores. In each core, the highest salinity, around 30 to 32 parts per thousand (ppt), was measured at the surface. These values are similar to bottom water salinities of Webb's Bay. Salinity then rapidly decreases downcore (Fig. 8B). In one core, salinity decreases to 7 ppt at 166-cm depth. Most of the cores exhibit salinity values below 20 ppt at depths exceeding 1 m.

Bottom water temperatures

A moored conductivity-temperature-depth (CTD) sensor deployed at 18-m water depth (CTDm in Fig. 1C) shows the variations in bottom water temperatures from September 2022 to November 2023 (Fig. 9A). From late July to mid-September, water at 18 m was at its warmest, with a mean of 7.3°C. In late September, temperatures gently decreased until they reached ≤0°C on 1 December. CTD profiles collected in early November 2023 showed a generally consistent water temperature from the surface to the bottom, averaging around 4°C (Fig. 9B). Temperatures continued slowly decreasing during the winter until they reached their minimum temperature of −1.69°C in March 2023. By the end of March, temperatures slowly started increasing again until they reached ≥0°C on 1 June. In July 2023, during core collection and bathymetric surveys, bottom waters were around 5.3°C at 18-m water depth.

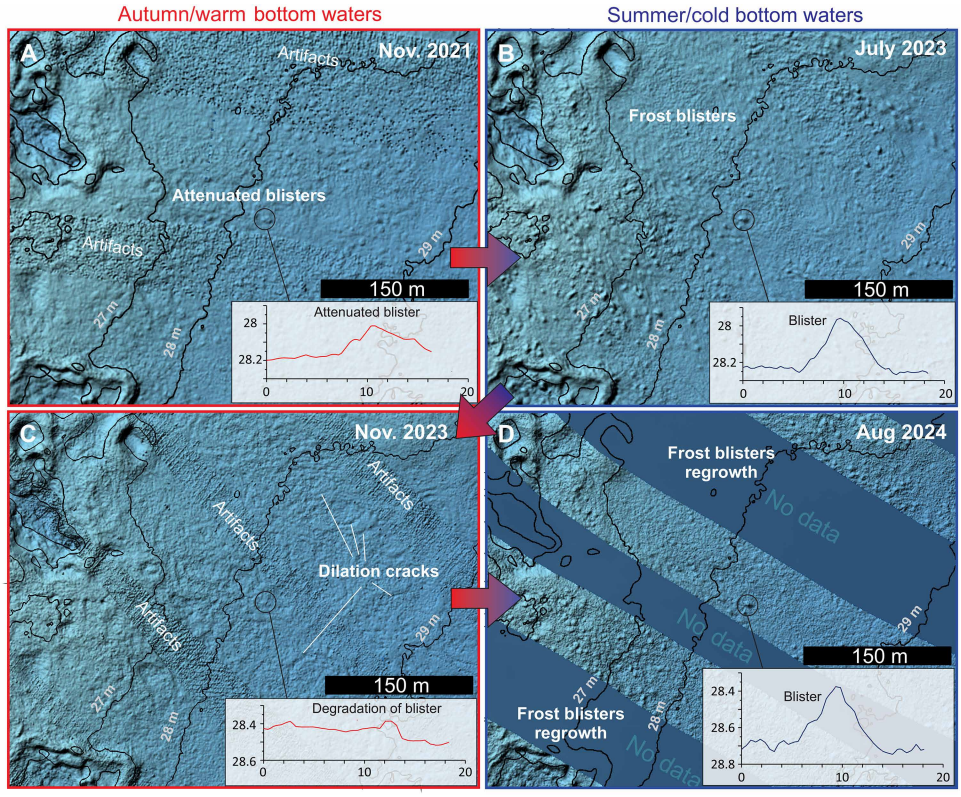

Fig. 5. Seasonal formation and degradation of blisters. Multibeam bathymetry in November 2021 (**A**), July 2023 (**B**), November 2023 (**C**), and August 2024 (**D**). Bottom waters in (A) and (C) were around 4°C, whereas they were near or below 0°C in (B) and (D). Red colors represent warm bottom waters, whereas blue colors represent cold bottom waters. Graphs have distance (meters) in the *x* axis and depth (meters) in the *y* axis. Circle with bathymetric profile represents the same zone from (A) to (D). Location in Fig. 3A.

We use a temperature-depth (TD) sensor moored at 60 m water depth in Nain Bay to estimate the bottom water temperature at 30-m depth in Webb's Bay. At 60-m water depth, temperatures remained ≤1°C for most of the year (median, −1.65°C). Temperatures increased above −1°C by late August and above 0°C by early October. They then decreased below 0° and −1°C in December and January, respectively. Temperatures stayed below −1°C for at least 6 to 7 months afterward. On the basis of CTD casts, we infer that the temperatures at 30-m depth remained below 0°C at least between December and July and increased to 4°C in September and October (Fig. 9A).

DISCUSSION

Evidence for SGD

The three types of pockmarks identified in Webb's Bay are attributed to SGD from meteoric recharge. SGD is supported by the presence of low salinity porewater near the seabed surface, attaining values as low as 7 ppt at 166-cm depth (Fig. 8). The absence of acoustic blanking in the zone of the pockmarks or thermokarst areas provides additional evidence that gas escape is not responsible for the presence of pockmarks (Fig. 4E). Acoustic blanking typically occurs where gas in sediment scatters and absorbs acoustic energy, leading to a loss of signal and creating a "blanked" area on the profile (*26*). In the pockmark area, acoustic penetration is continuous although slightly incoherent. SGD does not cause blanking because the acoustic signal is not severely affected by brackish water, except if seepage disturbs the sediment column.

Small pockmarks are predominantly found on bathymetric highs, notably on the Webb's Brook delta (Fig. 1C), and the ridges attributed to moraines (Fig. 3A). The regular pockmarks occur in similar locations but are less widespread. In these locations, submarine groundwater is discharging through the seafloor, with some focusing where the larger pockmarks are located. SGD occurs preferentially at these locations due to coarser sediment (till) being closer to the sediment-water interface and the thinning of glaciomarine mud that acts as an aquitard (Fig. 4E) (*8*). Thick glaciomarine mud increases hydraulic resistance to groundwater seepage, whereas thin layers allow groundwater to seep and fill the Holocene mud pore space. In deeper waters, fewer SGD-related pockmarks are visible (Fig. 3A), potentially due to shallow subsea freezing from contact with cold bottom waters, preventing active discharge, or the lower resolution of the seafloor bathymetry at depth, which precludes the mapping of the small pockmarks. Regardless, porewater salinity in the sediment cores indicates the presence of freshened groundwater throughout the head of Webb's Bay.

Stability of perennial subsea permafrost landforms between 2021 and 2024

Repeat seafloor mapping at the head of Webb's Bay revealed both perennial and seasonal features on the seafloor. No large-scale changes

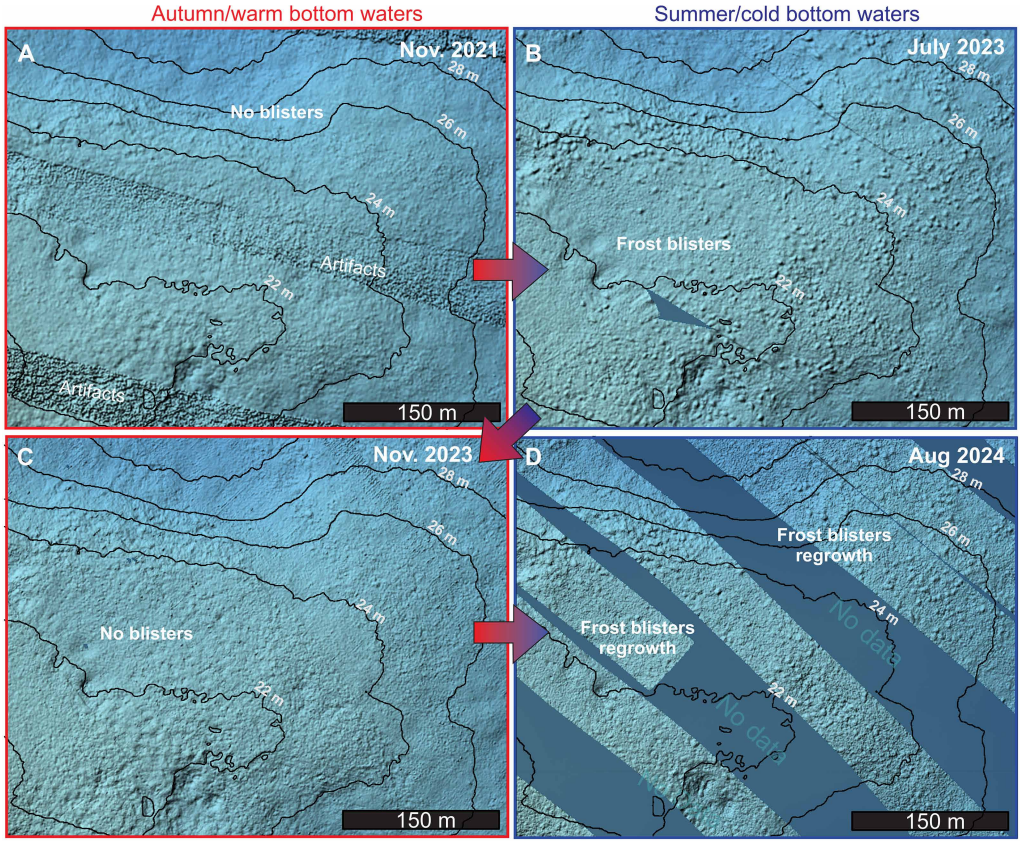

Fig. 6. Seasonal formation and degradation of blisters. Multibeam bathymetry in November 2021 (**A**), July 2023 (**B**), November 2023 (**C**), and August 2024 (**D**). Bottom waters in (A) and (C) were around 4°C, whereas they were near or slightly above 0°C in (B) and (D). Red colors represent warm bottom waters, whereas blue colors represent cold bottom waters. Location in Fig. 3A.

(>1-m vertical difference) were detected on the thermokarst or large frost mound areas during the 2021–2024 period. The absence of large-scale changes contrasts with similar thermokarst features in the Beaufort Sea that have changed by tens of meters over a 9-year period (*13*). The absence of substantial geomorphic change may be attributed to the current degraded state of subsea permafrost in Webb's Bay being closer to equilibrium with bottom water temperatures. If the permanently ice-bounded sediment maintains an average temperature below 0°C, then it may remain frozen.

The high-amplitude reflection linked to the permafrost table is buried under ~1 to 2 m of sediment. This sediment cover protects the ground ice from rapid changes in bottom-water temperatures during summer, preventing rapid ice melting. The insulation provided by sediment reduces heat transfer to the ice-bounded sediment, thereby protecting it from thawing and potentially attenuating any seasonal bottom-water temperature signals. Therefore, the larger landforms that appear somewhat buried are better protected from seasonal changes in water temperature. The insulating effect of sediment (and vegetation) on top of ground ice is well-known in terrestrial permafrost environments (*27*, *28*) and on debris-covered glaciers (*29*–*31*). Alternatively, large seabed changes might occur only in years with more marked changes in bottom water temperatures or over longer periods, neither of which were captured during the 3-year interval covered by our surveys.

Seasonality of subsea frost blisters

The small blisters on the seafloor of Webb's Bay are similar to frost blisters, icing blisters, or icing mounds observed in terrestrial environments (*32*). A frost blister is a cryogenic landform characterized by a localized mound or dome that forms in cold climates where the ground contains water (*32*–*34*). Frost blisters originate from the accumulation of groundwater in localized areas within a shallow subsurface layer. As temperatures drop, the water in the ground freezes and expands, creating upward pressure. The growth of a frost blister requires a continuous influx of water to the freezing area, supplied by surrounding unfrozen ground or through capillary action, where water ascends through the soil and freezes as the frost front descends (*32*). As more water freezes and expands, the blisters grow. The ice core at the center of the blister pushes the overlying soil and sediment upward, creating the dome shape. The height and size of the frost blister are determined by the amount of available water and the duration of freezing conditions. Frost blisters can develop quickly within a single cold season, as observed in Webb's Bay, but may also persist and grow over multiple seasons under favorable conditions. Unlike frost blisters, icing mounds and icing blisters are composed entirely of ice.

The small subsea frost blisters in Webb's Bay have dimensions comparable to those observed in terrestrial active layers and are interpreted as such. On the Mackenzie Delta, frost blisters identified by (*34*) are less than 1 m high and 3.7 to 8.5 m in diameter. These

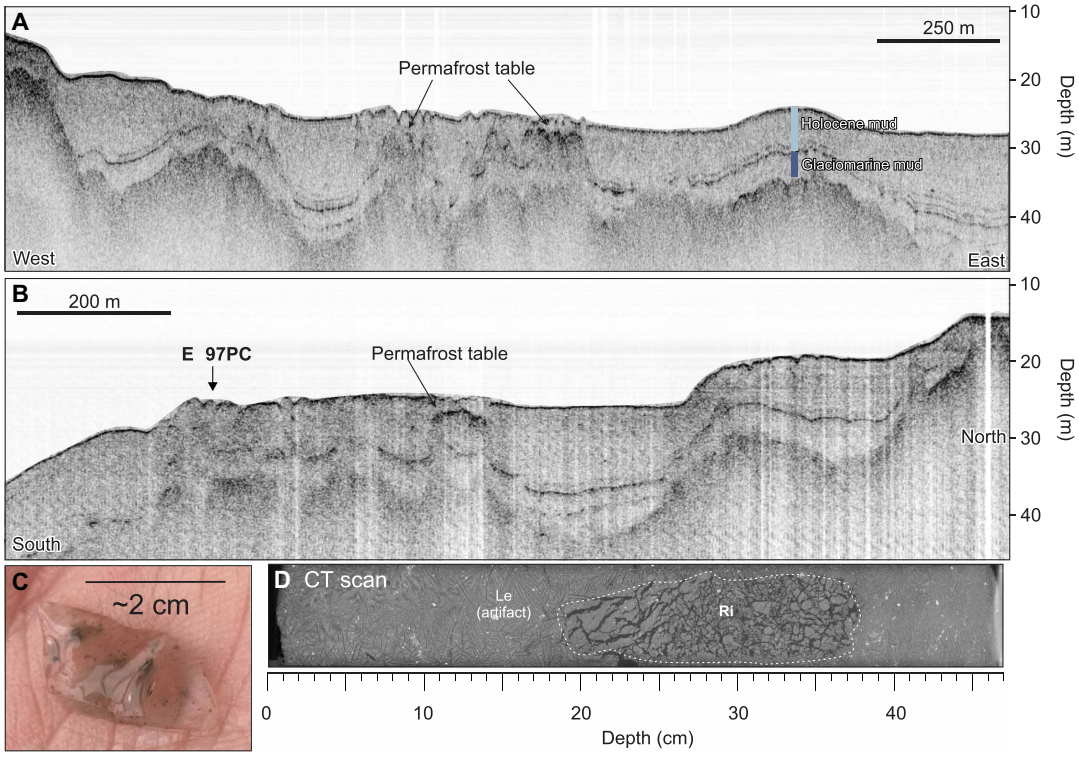

Fig. 7. Representative subbottom profiles and core imagery from the thermokarst area of Webb's Bay. (**A** and **B**) Subbottom profiles illustrating chaotic high-amplitude reflections attributed to discontinuous subsea permafrost. Frost mounds shown in Figs. 5 and 6 are widespread throughout these profiles, even if not visible at subbottom scale. (**C**) Ice recovered from a sediment core laying on the palm of a hand. (**D**) Ice lens in sediment core 97PC collected in Webb's Bay, including a computed tomography (CT) scan image of the upper section of core 97PC. Location of profiles in Fig. 3A. Location of core 97PC in Fig. 8. Irregular reticulate cryostructures (Ri) and lenticular cryostructures (Le), the latter being artifacts formed by the rapid freezing of sediment following core collection.

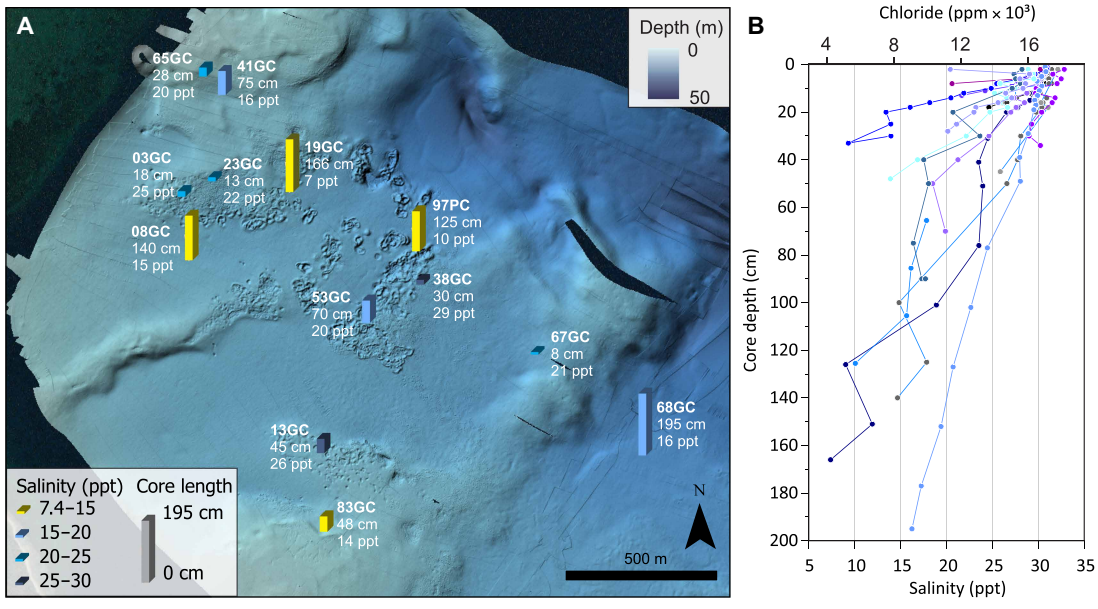

Fig. 8. Freshened porewater in marine sediment. (**A**) Distribution of sediment cores from which porewater chloride data were collected. Length of bars indicates the length of the cores, and the colors represent the lowest salinity value recorded at the base of the cores. Location is the same as Fig. 1D. (**B**) Salinity profiles of all thirteen cores collected. Colors represent individual cores.

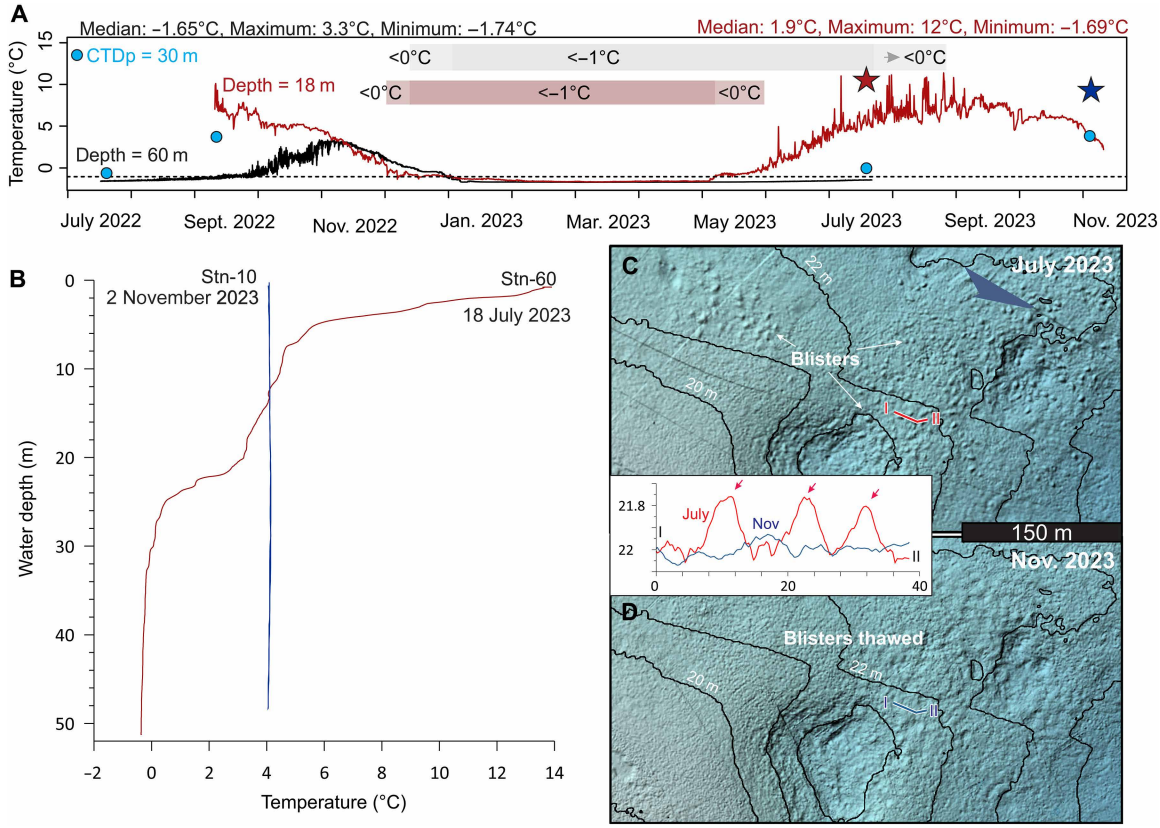

Fig. 9. Bottom water temperature of Webb's Bay. (**A**) Evolution of bottom water temperatures in Nain from July 2022 to November 2023 for water depths of 18 m (red) and 60 m (black). Blue dots are bottom water temperatures measured from CTD profiles (CTDp) at 30 m. Stars indicate the timing and bottom water temperatures from the CTD profiles shown in (B). Dashed line in (A) is −1°C isotherm at which porewater at a salinity of 20 ppt freezes (*50*). Horizontal gray and red bars indicate the time interval when bottom waters are below −1° and 0°C for water depths of 18 m (red) and 60 m (gray). (**B**) CTD profiles in July 2023 and November 2023 showing the warming of bottom waters and the cooling of surface waters throughout the autumn. (**C**) Multibeam bathymetry at 20-m water depth in July 2023, illustrating the presence of small frost blisters, which have thawed entirely by November 2023. (**D**) The graph illustrates the presence and absence of frost blisters for both months. The *x* axis is distance (meters), and the *y* axis is depth (meters). Location of (A) and (B) in Fig. 1C (CTDp and CTDm) and location of (C) and (D) in Fig. 3A.

frost blisters contain a core of ice that is 15 to 58 cm thick. Similarly, the subsea frost blisters in Webb's Bay measure about 5 m wide and 30 to 50 cm high. On the Mackenzie Delta, they form on saturated floodplains, which provide conditions favorable for frost blister growth during winter. They grow because of hydrostatic pressure, usually during a single winter (*34*). In Webb's Bay, most of the frost blisters observed in July 2023 formed during the winter of 2022–2023. Similarly, those observed in August 2024 were formed during the single winter of 2023–2024 (Figs. 5 and 6).

In terrestrial environments, seasonal frost blisters are often found in areas with thin, discontinuous permafrost. The permafrost table restricts super-permafrost groundwater flow to the shallow subsurface (*3*). Hydraulic transmissivity is reduced as the freezing front advances downward and thins the saturated, unfrozen zone, resulting in buildup of water and pressure (*32*). In Webb's Bay, this mechanism can potentially be involved in the formation of frost blisters over the apparent permafrost table (Fig. 7). There, the permafrost appears discontinuous, allowing upward movement of groundwater flow. The presence of the permafrost table or pereletok (frozen ground in areas free of permafrost) would prevent the freshened groundwater from flowing downward and cause saturation of freshened groundwater in the near-surface sediment. However, frost blisters are also observed where no apparent permafrost table is observed (Fig. 7). There, we assume that the freshened groundwater saturates the near surface through upward flow from buoyancy and/or the hydraulic head gradient.

Frost blister density on the Mackenzie Delta was observed in a slight topographic gradient, with increased soil moisture that controls ground ice distribution (*34*). Assuming a similar process in subsea environments, the denser distribution of frost blisters must be associated with higher groundwater discharge into Webb's Bay. This is apparent in the shallower waters where the frost blisters form close to the pockmark fields (Fig. 3A). In deeper water, the frost blisters are mostly concentrated near the subsea thermokarst area, suggesting either groundwater along the permafrost table or ground ice melt within the permafrost favoring the presence of freshened porewater near the surface. The latter process is similar to the process described by (*9*) where ground-ice melt at depth moves upward and refreezes near the surface, forming ice outcrops.

The backscatter results from November 2021 to August 2024 (fig. S1) show that low reflectivity associated with the frost blisters is fairly constant through time, even when frost blisters are not present. The persistence of low reflectivity spots suggests that these areas are saturated with freshened groundwater, which refreezes every

winter. High water content in surficial mud will produce low reflectivity compared to sand and gravel. When frost blisters are present, ice is covered by 20 cm of sediment, which is likely the reflecting surface. Ice is unlikely to be the reflecting surface because it would produce a high backscatter response.

Formation of subsea frost blisters

The seasonal formation and degradation of frost blisters is observed through repeat bathymetric surveys and supported by bottom water temperature monitoring (Figs. 9 and 10). The depth of seasonal freeze-thaw in the shallow subsurface can be estimated using the Stefan equation (*35*, *36*), with equation parameters and forcing data detailed in Supplementary Text. Although it is the most widely applied ground freeze-thaw equation (*36*), the Stefan equation has several limitations, including not directly accounting for the influence of subsidence or heave on the phase change front. Accordingly, the calculated seasonal frost and thaw depths should be considered first-order estimates. We used estimated values for thermal properties and the bottom water temperature time series in the deep and shallow water to calculate the seasonal freezing and thawing indexes. These indexes were calculated relative to the freezing temperatures, which were determined for porewater salinities of 20 and 10 ppt. For the ranges of depths, properties, and salinities considered, we found seasonal freezing depths in the bed of Webb's Bay that ranged from between 0.32 and 0.70 m. These values are in alignment with the depth of the seasonal frost layer identified in core 97PC where the base of the frost layer was at ~40 cm, within the range expected for the area. These maximum freezing depths are less than typical terrestrial active layer thicknesses in the subarctic or frost depths in southern Canada (*37*), but that is expected given that the freezing index for bottom seawater is much lower than that for air or ground water.

The Stefan equation application illustrates the potential depths of seasonal freeze-thaw and associated expansion and contraction. However, the calculated frost depth cannot explain the formation of the frost blisters themselves, which are 20 cm high. Water freezing and expanding at 9% over a defined area with a thickness of 0.5 m leads to an upward movement of only ≤0.05 m. Over the blisters, which have a height above seabed of about 0.2 m, an initial thickness of at least 2.2 m of porewater is required to freeze to create the dome-shape of the blisters, assuming that they form in a single freezing season, as seen between 2023 and 2024. This suggests that the surface manifestations of the blisters may form in a single season but that the underlying ground ice that forms the blisters may exist over multiple years.

Assuming porewater salinity of 20 ppt, the porewater starts to freeze at about −1.1°C. Bottom water temperatures were sustained below −1.1°C starting on 1 January 2023 at 18-m depth and warmed above that temperature on 8 May 2023. Therefore, in the shallower waters of Webb's Bay, porewater freezes at least during 4 months of the year before starting to thaw in the spring. In the deeper waters of Nain Bay (60 m deep), water temperatures dropped below −1.1°C starting in December and remained below that temperature until August 2023. At 30-m water depth, we estimated that temperatures would likely increase above −1°C in June/July or later (Fig. 9A). In July 2023 and August 2024, although bottom water temperatures were at 5°C, frost blisters were still observed (Figs. 5 and 6). The persistence of frost blisters over the summer indicates that the thawing front had not penetrated far into the sediment.

Degradation of subsea frost blisters

In November 2021, when bottom waters were warm, frost blisters were absent in water depth shallower than 25 m but were present, although attenuated, in the deeper parts of Webb's Bay (25 to 30 m). This suggests that deeper frost blisters located in the depth range of

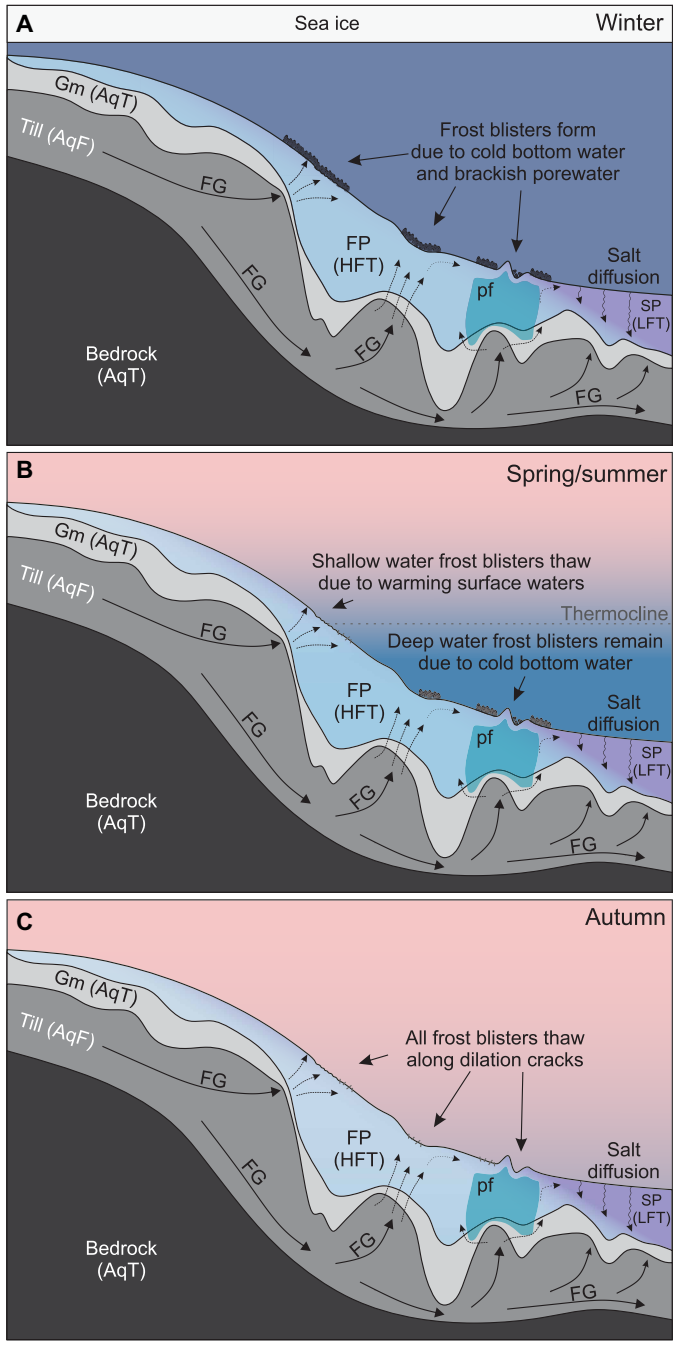

Fig. 10. Seasonal ground freezing in subsea thermokarst environment. (**A**) Formation of frost blisters during the winter season due to cold bottom water temperature and freshened groundwater discharge. (**B**) Thawing of frost blisters in shallow water due to warming of surface waters. (**C**) Thawing of all frost blisters due to warming of water column during autumn. Gm, glaciomarine mud; AqT, aquitard; AqF, aquifer; FG, freshened groundwater; FP, fresh porewater; SP, saline porewater; HFT, high freezing temperature; LFT, low freezing temperature; pf, permafrost.

the CIL may persist over multiple years and thaw during warmer years, whereas shallow blisters are seasonal. For example, although characterized by a normal CIL earlier during the year, 2023 was a warm year where multiple high-intensity marine heat waves affected surface waters of Labrador (*38*). The accumulated heat in the surface likely mixed with the deeper waters of Webb's Bay during the late summer and fall, leading to the degradation of all frost blisters by November 2023 (Figs. 5, 6, and 10).

During the summer and fall of 2023, frost blisters degraded along dilation cracks (Fig. 5C). In terrestrial environments, these cracks are opened during the summer by hydrostatic uplift as the frozen overburden rises during blister growth (*39*, *40*). A similar mechanism appears evident on the seabed of Webb's Bay as evidenced by many cracks where frost blisters have thawed (Fig. 5C). As dilation cracks form during the freezing, they also create pathways for warmer summer and fall waters to interact with the ice core through advection. As warm water melts the ice core, frost blisters thaw and create a heaved topography with dilation cracks. This topography is widespread at the head of Webb's Bay, indicating that this process was far more common before 2021 (Fig. 3A). Such cracks or related "macropores" have been shown to provide preferential pathways for groundwater flow in terrestrial environments with freeze-thaw (*41*) and may alter local submarine groundwater flow paths.

Seasonal frost blisters, forming near the seabed surface, rapidly respond to changes in bottom water temperatures. These blisters have a thinner sediment cover (≤30 cm according to frost depth in core; Fig. 7D), providing minimal insulation against temperature fluctuations. This lack of substantial insulation allows heat from warming waters during the summer and fall to quickly reach the underlying ice core of the frost mounds (Fig. 10). The maximum summer thaw depth calculated using the Stefan equation in shallow waters (Supplementary Text) exceeds the thickness of the sediment cover overlying the massive ice. In addition, the near-surface formation of frost blisters increases the likelihood of direct exposure of core ice to bottom waters. Direct exposure of ice to the seafloor was observed in the Beaufort Sea (*9*). This proximity of ice to saline bottom waters allows bottom water thermal regime shifts to affect the ice core more quickly and intensely.

Smaller frost blisters have a higher surface area-to-volume ratio compared to larger perennial landforms, meaning that a larger proportion of the frost blister volume is exposed to the warmer bottom temperatures. This higher ratio facilitates more efficient heat transfer between the surrounding sediment and the ice core, resulting in faster thermal responses. While only vertical heat transfer and phase change were considered in our first-order Stefan analysis, it is likely that horizontal heat transfer is an important thaw mechanism for both seasonal and perennial ground ice features. This is similar to how horizontal conduction has been shown to exert strong control on the thaw rates for permafrost islands (peat plateaus) in terrestrial settings (*42*, *43*). It is also possible that tidal pumping of the unfrozen sediment during the fall causes high rates of vertical water exchange and concomitant heat advection that would accelerate thaw.

Sorted polygons formed from freeze-thaw cycles?

In addition to the frost blisters, the backscatter data of Webb's Bay revealed high-reflectivity polygons throughout the head of Webb's Bay (Fig. 2 and 3B) that are not observed outside of this region. As such, their genesis is also assumed to be related to freeze-thaw cycles. These polygons appear to be composed of gravel and mud, resembling sorted circles found on land that result from freeze-thaw cycles (*44*). During freezing, water in the soil expands, causing the ground to heave. In poorly sorted sediment, this expansion causes differential movement, with larger particles like gravel rising more easily than finer particles. Repeated freezing and thawing causes larger particles to gradually migrate to the surface and edges of the heaving area, while finer particles settle in the lower and central areas. Over time, this differential movement and sorting of particles create distinct patterns with gravel and larger particles forming small, typically circular or polygonal aggregations surrounded by finer sediments. This process of sorted polygon formation provides a plausible explanation for the presence of these high-reflectivity polygons in Webb's Bay.

Regional and global implications of seasonal expansion and contraction of the seafloor

Seafloor mapping in Webb's Bay has led to the discovery of landforms associated with subsea permafrost and seasonal ground freezing. While (*8*) previously identified perennial landforms, this study marks the first observation of landforms related to seasonal ground freezing. These seasonal features, like their perennial counterparts (thermokarst and frost mounds), are primarily influenced by bottom water temperatures and SGD, which affects the equilibrium freezing temperatures. These data show that the interaction between freshened porewater and cold bottom waters leads to seasonal seafloor expansion and contraction through the formation and degradation of frost blisters, a process previously undocumented through geomorphic and oceanographic observations. This process may represent a potential hazard in many regions with cold bottom waters. Seafloor expansion and contraction due to subsea ground freezing and active layer processes likely represents a geohazard for offshore infrastructure. Repeated strain from expansion and contraction could accelerate damage to underwater cables. Minor vertical movements can stress cable joints and connections, increasing the likelihood of breaks at these points and can cause cable stretching or sagging, raising the risk of physical damage. Consequently, these previously unrecognized processes could threaten offshore infrastructure.

The detection of seasonal seafloor expansion and contraction in Webb's Bay was only possible because of the very high-resolution mapping of the seabed. With a coarser resolution gridded surface, these frost blisters would not have been recognized (*8*). Given that most nearshore areas in the world are gridded at horizontal resolution greater than 2 m and that most publicly available datasets are made available at resolution coarser than 10 m, there is a high likelihood that similar seasonal features cannot be resolved in most available datasets. In addition, if seafloor mapping is done during the late summer and fall, when navigation is facilitated by the absence of sea ice, then frost blisters are less likely to be present due to ongoing thaw. Therefore, the timing of surveys, combined with the seasonality and size of these features, makes their recognition challenging in many regions using standard seafloor mapping techniques. These processes and landforms may be ongoing but undetected in many areas, warranting consideration in offshore infrastructure planning. Although this study identified processes in a subsea thermokarst environment, subsea permafrost is not a prerequisite for seasonal seafloor expansion and contraction. Thus, these dynamics have the potential to affect high to mid-latitude regions where seasonal cold

bottom waters exist. This represents a large gap in assessing the distribution of ground freezing processes and landforms, leading to seafloor expansion and contraction. It is worth noting that ice has been observed in nearshore marine sediments in Hudson Bay (*45*) and Cambridge Fjord, Nunavut (*46*), suggesting that similar seasonal cryospheric processes could be widespread in areas where bottom waters are seasonally <0°C. Furthermore, the temperature threshold for seasonal freeze-thaw in subsea sediment can be increased in locations where freshened SGD affects the freezing point.

Seasonal changes in seabed composition driven by freeze-thaw cycles are also likely to affect benthic ecosystems by altering biophysical conditions, oxygen levels through limiting porewater exchange and nutrient availability (*47*). In Webb's Bay, while local microbial communities remain unexplored, sparse macrofaunal communities were reported (*48*), possibly reflecting the environmental constraints imposed by these dynamic processes. This underscores the need for further research to understand both the short- and long-term effects of freeze-thaw cycles on seasonal and perennial ground ice features in thermokarst environments, and their influence on benthic ecosystem functioning. Such knowledge is essential for scaling localized seabed processes to broader regional and global ecological frameworks.

MATERIALS AND METHODS

Hydroacoustic surveys

Four multibeam bathymetric surveys were conducted in Webb's Bay in October 2021, July 2023, November 2023, and August 2024. All four surveys were conducted using different versions of the Kongsberg EM-2040 on board the *RV Ludy Pudluk* (2021 and 2024), *RV William-Kennedy* (July 2023), and *RV Nuliajuk* (November 2023). The multibeam echo sounders operated at a variable frequency of 200 to 400 kHz. Data were corrected for tides measured by the Canadian Hydrographic Service at the Nain station, 25 km from Webb's Bay. Raw soundings were corrected for sound velocity variations in the water column. The multibeam bathymetric data were then processed using Caris HIPS and SIPS 11.4 software to correct for tide elevation and vessel movement (roll, pitch, heave, and yaw) during acquisition and allowed the creation of a 25- to 50-cm gridded surface of Webb's Bay seabed.

Subbottom profiles were collected using a 3.5-kHz Knudsen Pinger on board the *RV Nuliajuk* (2021 and 2023) and the *RV William-Kennedy* (July 2022). The Pinger offers a vertical resolution of about 10 cm and between 0- and 30-m penetration in fine-grained sediment. A sound speed of 1500 m/s was used to determine approximate depth of seafloor and subbottom sediment.

In situ water column temperature

CTD profiles were collected during the four different cruises, except for November 2021. CTD profiling of the water column in July 2022 and July 2023 was done using a stand-alone Seabird 19plusV2 SeaCAT profiler (CTDp in Fig. 1C). In September 2022, a RBR Concerto was used over the same locations as the July 2022 CTD profiles. In November 2023 and August 2024, an AML X2Xhange CTD was used from the *RV Nuliajuk* and the *RV Ludy-Pudluk*.

In addition to water column profiling, CTDs were moored in Webb's and Nain Bay (Fig. 1). In September 2022, a RBR Duet TD sensor was deployed in 17.5-m water depth near Webb's brook (56.8027°N, 61.9088°W). This TD sensor recorded the temperature and tidal variations of bottom waters for an entire year, until it was recovered in November 2023. It covers the temperature variations between the July 2023 and November 2023 multibeam surveys.

A RBR CTD was deployed at 30-m water depth in the subsea permafrost area from March 2023 to November 2023. However, this mooring was not recovered because of acoustic release issues. Therefore, to understand the water temperature variations at depth, we used the data from a RBR TD installed on a mooring line in Nain Bay, at 60-m water depth. Although twice the depth of the Webb's Bay mooring, it allows us to compare bottom water thermal regimes from the shallow water mooring described above. This mooring recorded water temperature variations from July 2022 to July 2023, illustrating temperature evolution over the fall and winter seasons.

Sedimentology and porewater analyses

Sediment gravity cores were collected from the *RV William-Kennedy* in 2023 using a 2-m-long Mooring Systems Inc. gravity corer. Core 2023002-97PC (130.5 cm long, 56.78°N, 61.89°W) was collected in July 2023 over the thermokarst area, and a frozen sample was observed through the liner in the upper section. The top section of the core was kept frozen in a −20°C freezer to preserve cryostructures while the bottom section was kept at 4°C. The internal structures of the frozen sediment sample were then imaged at the Bedford Institute of Oceanography using a Geotek X-ray Computed Tomography system. Sixteen-bit tiff slices, ranging in grayscale depth from 0 to 65535, were imported into open-source three-dimensional (3D) visualization software (Slicer3D) to reconstruct a 3D volume.

Thirteen sediment gravity cores were collected in July 2023 near pockmarks and permafrost mounds to assess the downcore evolution of porewater chloride content and estimate salinity. Upon core recovery, porewater was extracted and filtered (0.15 μm) using Rhizon samplers inserted through holes drilled down the side of the core liner. Porewater was extracted at 2-cm resolution to a downcore core depth of 20 cm and increasingly coarser resolution below. Samples were then frozen until analysis. Chloride content was determined by ion chromatography with a Dionex Aquion IC system following a 1:1000 sample dilution. Reproducibility on replicate samples was <1%.

Supplementary Materials

This PDF file includes:

Supplementary Text
Fig. S1
References

REFERENCES AND NOTES

1. J. A. Heginbottom, J. Brown, E. S. Melnikov, O. J. Ferrians Jr., "Circumarctic map of permafrost and ground ice conditions," in *Proceedings of the Sixth International Conference on Permafrost* (South China University of Technology Press Wushan Guangzhou, China, 1993), vol. 2, pp. 1132–1136.
2. E. A. G. Schuur, B. W. Abbott, R. Commane, J. Ernakovich, E. Euskirchen, G. Hugelius, G. Grosse, M. Jones, C. Koven, V. Leshyk, D. Lawrence, M. M. Loranty, M. Mauritz, D. Olefeldt, S. Natali, H. Rodenhizer, V. Salmon, C. Schädel, J. Strauss, C. Treat, M. Turetsky, Permafrost and climate change: Carbon cycle feedbacks from the warming arctic. *Annu. Rev. Env. Resour.* **47**, 343–371 (2022).
3. M. A. Walvoord, B. L. Kurylyk, Hydrologic impacts of thawing permafrost—A review. *Vadose Zone J.* **15**, 1–20 (2016).
4. J. Hjort, D. Streletskiy, G. Doré, Q. Wu, K. Bjella, M. Luoto, Impacts of permafrost degradation on infrastructure. *Nat. Rev. Earth Environ.* **3**, 24–38 (2022).

5. S. S. Sayedi, B. W. Abbott, B. F. Thornton, J. M. Frederick, J. E. Vonk, P. Overduin, C. Schädel, E. A. G. Schuur, A. Bourbonnais, N. Demidov, A. Gavrilov, S. He, G. Hugelius, M. Jakobsson, M. C. Jones, D. Joung, G. Kraev, R. W. Macdonald, A. David McGuire, C. Mu, M. O'Regan, K. M. Schreiner, C. Stranne, E. Pizhankova, A. Vasiliev, S. Westermann, J. P. Zarnetske, T. Zhang, M. Ghandehari, S. Baeumler, B. C. Brown, R. J. Frei, Subsea permafrost carbon stocks and climate change sensitivity estimated by expert assessment. *Environ. Res. Lett.* **15**, 124075 (2020).
6. P. Rekant, H. A. Bauch, T. Schwenk, A. Portnov, E. Gusev, V. Spiess, G. Cherkashov, H. Kassens, Evolution of subsea permafrost landscapes in Arctic Siberia since the Late Pleistocene: A synoptic insight from acoustic data of the Laptev Sea. *Arktos* **1**, 11 (2015).
7. M. Angelopoulos, P. P. Overduin, F. Miesner, M. N. Grigoriev, A. A. Vasiliev, Recent advances in the study of Arctic submarine permafrost. *Permafr. Periglac. Process.* **31**, 442–453 (2020).
8. A. Normandeau, J. B. R. Eamer, R. G. Way, E. J. Harrison, F. Cyr, C. K. Algar, J. L. Eamer, H. D. Geizer, J. Haddock, B. L. Kurylyk, N. Van Nieuwenhove, L. Pijogge, G. Philibert, K. Robert, M. Saunders, J. Tamborski, A. Limoges, Evidence for subsea permafrost in subarctic Canada linked to submarine groundwater discharge. *Nat. Geosci.* **17**, 1022–1030 (2024).
9. C. K. Paull, J. K. Hong, D. W. Caress, R. Gwiazda, J.-H. Kim, E. Lundsten, J. B. Paduan, Y. K. Jin, M. J. Duchesne, T. S. Rhee, V. Brake, J. Obelcz, M. A. L. Walton, Massive ice outcrops and thermokarst along the arctic shelf edge: By-products of ongoing groundwater freezing and thawing in the sub-surface. *J. Geophys. Res. Earth* **129**, e2024JF007719 (2024).
10. M. Angelopoulos, S. Westermann, P. Overduin, A. Faguet, V. Olenchenko, G. Grosse, M. N. Grigoriev, Heat and salt flow in subsea permafrost modeled with CryoGRID2. *J. Geophys. Res. Earth* **124**, 920–937 (2019).
11. M. Arboleda-Zapata, M. Angelopoulos, P. P. Overduin, G. Grosse, B. Jones, J. Tronicke, Exploring the capabilities of electrical resistivity tomography to study subsea permafrost. *Cryosphere* **16**, 4423–4445 (2022).
12. M. J. Duchesne, G. Fabien-Ouellet, J. Bustamante, Detecting subsea permafrost layers on marine seismic data: An appraisal from forward modelling. *Near Surf. Geophys.* **21**, 3–20 (2023).
13. C. K. Paull, S. R. Dallimore, Y. K. Jin, D. W. Caress, E. Lundsten, R. Gwiazda, K. Anderson, J. Hughes Clarke, S. Youngblut, H. Melling, Rapid seafloor changes associated with the degradation of Arctic submarine permafrost. *Proc. Natl. Acad. Sci. U.S.A.* **119**, e2119105119 (2022).
14. P. P. Bonnaventure, S. F. Lamoureux, The active layer: A conceptual review of monitoring, modelling techniques and changes in a warming climate. *Progr. Phys. Geog. Earth Environ.* **37**, 352–376 (2013).
15. W. Dobinski, Permafrost. *Earth Sci. Rev.* **108**, 158–169 (2011).
16. J. Hjort, O. Karjalainen, J. Aalto, S. Westermann, V. E. Romanovsky, F. E. Nelson, B. Etzelmüller, M. Luoto, Degrading permafrost puts Arctic infrastructure at risk by mid-century. *Nat. Commun.* **9**, 5147 (2018).
17. P. Lamontagne-Hallé, J. M. McKenzie, B. L. Kurylyk, S. C. Zipper, Changing groundwater discharge dynamics in permafrost regions. *Environ. Res. Lett.* **13**, 084017 (2018).
18. T. Zhang, Influence of the seasonal snow cover on the ground thermal regime: An overview. *Rev. Geophys.* **43**, RG4002 (2005).
19. T. E. Osterkamp, G. C. Baker, W. D. Harrison, T. Matava, Characteristics of the active layer and shallow subsea permafrost. *J. Geophys. Res. Oceans* **94**, 16227–16236 (1989).
20. M. Angelopoulos, P. P. Overduin, S. Westermann, J. Tronicke, J. Strauss, L. Schirrmeister, B. K. Biskaborn, S. Liebner, G. Maksimov, M. N. Grigoriev, G. Grosse, Thermokarst lake to lagoon transitions in eastern Siberia: Do submerged taliks refreeze? *J. Geophys. Res. Earth* **125**, e2019JF005424 (2020).
21. J. Deborde, P. Anschutz, I. Auby, C. Glé, M.-V. Commarieu, D. Maurer, P. Lecroart, G. Abril, Role of tidal pumping on nutrient cycling in a temperate lagoon (Arcachon Bay, France). *Mar. Chem.* **109**, 98–114 (2008).
22. P. U. Clark, W. W. Fitzhugh, Late deglaciation of the central Labrador coast and its implications for the age of glacial lakes Naskaupi and McLean and for prehistory. *Quatern. Res.* **34**, 296–305 (1990).
23. M. Vacchi, S. E. Engelhart, D. Nikitina, E. L. Ashe, W. R. Peltier, K. Roy, R. E. Kopp, B. P. Horton, Postglacial relative sea-level histories along the eastern Canadian coastline. *Quat. Sci. Rev.* **201**, 124–146 (2018).
24. B. Petrie, S. Akenhead, J. Lazier, J. Loder, The cold intermediate layer on the Labrador and northeast Newfoundland Shelves, 1978-1986. *NAFO Sci. Counc. Stud.* **12**, 57–69 (1988).
25. C. Florindo-López, S. Bacon, Y. Aksenov, L. Chafik, E. Colbourne, N. P. Holliday, Arctic ocean and hudson bay freshwater exports: New estimates from seven decades of hydrographic surveys on the Labrador shelf. *J. Climate* **33**, 8849–8868 (2020).
26. D. B. Albert, C. S. Martens, M. J. Alperin, Biogeochemical processes controlling methane in gassy coastal sediments—Part 2: Groundwater flow control of acoustic turbidity in Eckernförde Bay Sediments. *Cont. Shelf Res.* **18**, 1771–1793 (1998).
27. M. T. Jorgenson, V. Romanovsky, J. Harden, Y. Shur, J. O'Donnell, E. A. G. Schuur, M. Kanevskiy, S. Marchenko, Resilience and vulnerability of permafrost to climate change. *Can. J. For. Res.* **40**, 1219–1236 (2010).
28. Y. L. Shur, M. T. Jorgenson, Patterns of permafrost formation and degradation in relation to climate and ecosystems. *Permafr. Periglac. Process.* **18**, 7–19 (2007).
29. C. L. Fyffe, B. W. Brock, M. P. Kirkbride, D. W. F. Mair, N. S. Arnold, C. Smiraglia, G. Diolaiuti, F. Diotri, Do debris-covered glaciers demonstrate distinctive hydrological behaviour compared to clean glaciers? *J. Hydrol.* **570**, 584–597 (2019).
30. T. D. Reid, M. Carenzo, F. Pellicciotti, B. W. Brock, Including debris cover effects in a distributed model of glacier ablation. *J. Geophys. Res. Atmos.* **117**, D18105 (2012).
31. N. Reznichenko, T. Davies, J. Shulmeister, M. McSaveney, Effects of debris on ice-surface melting rates: An experimental study. *J. Glaciol.* **56**, 384–394 (2010).
32. W. H. Pollard, Seasonal frost mounds. *Can. Geogr. Géogr. Can.* **35**, 214–218 (1991).
33. S. Harris, H. French, J. Heginbottom, G. Johnston, B. Ladanyi, D. Sego, R. Everdingen, "Glossary of permafrost and related ground-ice terms" (Technical Memorandum No. 142, National Research Council of Canada, 1988).
34. P. D. Morse, C. R. Burn, Perennial frost blisters of the outer Mackenzie Delta, western Arctic coast, Canada. *Earth Surf. Process. Landf.* **39**, 200–213 (2014).
35. B. L. Kurylyk, M. Hayashi, Improved Stefan equation correction factors to accommodate sensible heat storage during soil freezing or thawing. *Permafr. Periglac. Process.* **27**, 189–203 (2016).
36. D. Riseborough, N. Shiklomanov, B. Etzelmüller, S. Gruber, S. Marchenko, Recent advances in permafrost modelling. *Permafr. Periglac. Process.* **19**, 137–156 (2008).
37. O. B. Andersland, B. Ladanyi, *Frozen Ground Engineering* (Wiley, ed. 2, 2003); www.wiley.com/en-us/Frozen+Ground+Engineering%2C+2nd+Edition-p-9780471615491.
38. N. Soontiens, H. J. Andres, J. Coyne, F. Cyr, P. S. Galbraith, J. Penney, An analysis of the 2023 summer and fall marine heat waves on the Newfoundland and Labrador Shelf: The impact of stratification, winds, and advection. State of the Planet Discussion [Preprint] (2025). https://sp.copernicus.org/preprints/sp-2024-5/.
39. H. M. French, Ice cored mounds and patterned ground, southern banks island, western canadian arctic. *Geogr. Ann. Ser. A Phys. Geogr.* **53**, 32–38 (1971).
40. K. M. Hinkel, F. E. Nelson, S. I. Outcalt, Frost mounds at Toolik Lake, Alaska. *Phys. Geogr.* **8**, 148–159 (1987).
41. A. A. Mohammed, B. L. Kurylyk, E. E. Cey, M. Hayashi, Snowmelt infiltration and macropore flow in frozen soils: Overview, knowledge gaps, and a conceptual framework. *Vadose Zone J.* **17**, 180084 (2018).
42. B. L. Kurylyk, M. Hayashi, W. L. Quinton, J. M. McKenzie, C. I. Voss, Influence of vertical and lateral heat transfer on permafrost thaw, peatland landscape transition, and groundwater flow. *Water Resour. Res.* **52**, 1286–1305 (2016).
43. Y. Wang, R. G. Way, J. Beer, A. Forget, R. Tutton, M. C. Purcell, Significant underestimation of peatland permafrost along the Labrador Sea coastline in northern Canada. *Cryosphere* **17**, 63–78 (2023).
44. A. Lewkowicz, S. Wolfe, V. Roujanski, E. Hoeve, S. Gruber, P. Roy-Léveillée, N. Brown, C. Koenig, H. Brooks, A. Rudy, P. Bonnaventure, M. Paquette, An Illustrated Permafrost Dictionary [Canadian Permafrost Association (CPA), 2024]; https://doi.org/10.52381/CPA.permafrostdictionary.1.
45. C. Fraser, "L'évolution morphologique et le développement stratigraphique des dépôts littoraux en milieu de régression forcée à Umiujaq, Baie d'Hudson," thesis, Université du Québec à Rimouski (2001).
46. R. Gilbert, D. L. Naldrett, V. V. Horvath, Holocene sedimentary environment of Cambridge Fiord, Baffin Island, Northwest Territories. *Can. J. Earth Sci.* **27**, 271–280 (1990).
47. J. G. Ernakovich, R. A. Barbato, V. I. Rich, C. Schädel, R. E. Hewitt, S. J. Doherty, E. D. Whalen, B. W. Abbott, J. Barta, C. Biasi, C. L. Chabot, J. Hultman, C. Knoblauch, M. C. Y. L. Vetter, M.-C. Leewis, S. Liebner, R. Mackelprang, T. C. Onstott, A. Richter, U. M. E. Schütte, H. M. P. Siljanen, N. Taş, I. Timling, T. A. Vishnivetskaya, M. P. Waldrop, M. Winkel, Microbiome assembly in thawing permafrost and its feedbacks to climate. *Glob. Chang. Biol.* **28**, 5007–5026 (2022).
48. Z. MacMillan-Kenny, M. Denniston, E. Edinger, A. Templeton, D. Côté, A. Limoges, K. Robert, Associations between iKaluk/Arctic charr (*Salvelinus alpinus*) and estuarine benthic diatom habitats in nearshore Nunatsiavut waters. *Polar Biol.* **48**, 20 (2025).
49. P. P. Overduin, T. S. von Deimling, F. Miesner, M. N. Grigoriev, C. Ruppel, A. Vasiliev, H. Lantuit, B. Juhls, S. Westermann, Submarine permafrost map in the Arctic modeled using 1-D transient heat flux (supermap). *J. Geophys. Res. Oceans* **124**, 3490–3507 (2019).
50. N. P. Fofonoff, R. C. Millard, "Algorithms for computation of fundamental properties of seawater" (UNESCO Technical Papers in Marine Sciences, 1983); https://doi.org/10.25607/OBP-1450.
51. R. Usbeck, M. Dillon, N. Kaul, A. Lohrberg, F. Nehring, A. C. Ploetz, High variability and exceptionally low thermal conductivities in nearshore sediments: A case study from the Eckernförde Bay. *Mar. Geophys. Res.* **44**, 24 (2023).
52. B. L. Kurylyk, K. T. B. MacQuarrie, J. M. McKenzie, Climate change impacts on groundwater and soil temperatures in cold and temperate regions: Implications, mathematical theory, and emerging simulation tools. *Earth Sci. Rev.* **138**, 313–334 (2014).

Acknowledgments: We thank K. Regular and A. Templeton for surveys on the *RV Ludy-Pudluk* and *RV Nuliajuk* as well as all the crew and scientific participants of the 2022

and 2023 *RV William-Kennedy* cruises. We would also like to acknowledge the Nunatsiavut Government, the Nunatsiavut Research Centre, and the Labrador Inuit of Nain for their guidance on research conducted on traditional Inuit lands. **Funding:** This project was funded by the Marine Geoscience for Marine Spatial Planning of the Geological Survey of Canada and the Natural Science and Engineering Research Council of Canada Ship-time allocation grant. Work on the *RV William-Kennedy* was supported, in part, by the Churchill Marine Observatory, a Canada Foundation for Innovation grant led by the University of Manitoba in collaboration with other partners, including the Arctic Research Foundation. This work was completed with Nunatsiavut government Research Advisory Committee (NGRAC) approval nos. 18034796 and 11666556. **Author contributions:** Conceptualization: A.N. and B.L.K. Methodology: A.N., B.L.K., and A.L. Investigation: All authors. Visualization: A.N. Writing—original draft: A.N. and B.L.K. Writing—review and editing: All authors. **Competing interests:** The authors declare that they have no competing interests. **Data and materials availability:** All data needed to evaluate the conclusions in the paper are present in the paper and/or the Supplementary Materials and can be found in the Federated Research Data Repository (FRDR): DOI: 10.20383/103.01363.

Submitted 15 February 2025
Accepted 2 October 2025
Published 29 October 2025
10.1126/sciadv.adw7439